Isomorphic substitution of aluminium by iron into single-walled alumino-silicate nanotubes: A physico-chemical insight into the structural and adsorption properties of Fe-doped imogolite

(Article begins on next page)

08 November 2024

The publisher's version is available at:
http://linkinghub.elsevier.com/retrieve/pii/S1387181115006514

When citing, please refer to the published version.

Link to this full text:
http://hdl.handle.net/2318/1638449

iris - AperTO

Isomorphic substitution of aluminium by iron into single-walled alumino-silicate nanotubes: a physico-chemical insight into the structural and adsorption properties of Fe-doped imogolite.

E. Shafia,[a] S. Esposito,[b] M. Armandi,[a] M. Manzoli,[c] E. Garrone[a] and B. Bonelli[a,*]

[a] *Department of Applied Science and Technology and INSTM Unit of Torino Politecnico, Corso Duca degli Abruzzi 24, Politecnico di Torino, Turin, Italy.*

[b] *Department of Civil and Mechanical Engineering, Università degli Studi di Cassino e del Lazio Meridionale, Via G. Di Biasio 43, 03043 Cassino (FR), Italy.*

[c] *Department of Chemistry & NIS Interdepartmental Centre, University of Turin, Via P. Giuria 7, 10125 Turin, Italy.*

* *Corresponding author: Tel. +39 011 0904719 Fax. +39 011 0904624; e-mail: barbara.bonelli@polito.it (Prof. Barbara Bonelli).*

Abstract

Morphological, textural and surface properties are reported of Fe-doped aluminosilicate nanotubes (NTs) of the imogolite type (IMO, $(OH)_3Al_2O_3SiOH$). Two samples with 1.4 wt. % Fe were obtained by either direct synthesis (Fe-1.4-IMO) or post synthesis loading (Fe-L-IMO). Since formation of Fe_2O_3 clusters was observed in both cases, a third sample with a lower Fe content corresponding to 0.70 wt. % Fe was prepared by direct synthesis, with the aim of preventing clusters formation (Fe-0.70-IMO). The samples were characterized by: High Resolution Transmission Electron Microscopy (HRTEM); X-ray Diffraction (XRD); N_2 sorption isotherms; Thermo-Gravimetric Analysis (TGA); Diffuse Reflectance (DR) UV-Vis and IR spectroscopies; electrophoretic mobility in water (ζ-potential) and adsorption of the azo-dye Acid Orange 7 (NaAO7) from water solutions. With Fe-0.70-IMO, Al^{3+} isomorphic substitution by Fe^{3+} was the main process occurring, leading to a material with formula $(OH)_3Al_{1.975}Fe_{0.025}O_3SiOH$, in which formation of Fe(OH)Al groups occurred at NTs outer surface. With Fe-1.4-IMO, some of the formed Fe(OH)Al groups probably acted as nucleation seeds, due to the natural tendency of iron to form Fe-O-Fe bridges, being responsible of the (undesired) formation of some Fe_2O_3 clusters. Comparison with Fe-L-IMO, in which only the formation of Fe_2O_3 clusters was, in principle, expected, showed on the contrary that some isomorphic substitution occurred also by post-synthesis loading.

The intrinsic acidity of Fe(OH)Al groups was marginally different from that of Al(OH)Al groups, as shown by both IR spectroscopy and ζ-potential measurements, but the presence of iron modified the adsorption properties of IMO. Interaction with $AO7^-$ anions in water, indeed, occurred in different ways: i) with proper IMO, besides electrostatic interaction with the positively charged external surface of nanotubes, $AO7^-$ anions preferentially adsorb via H-bonding on inner SiOH groups; ii) with both Fe-0.70-IMO and Fe-1.4-IMO, Fe^{3+} cations of Fe(OH)Al groups act as coordination centres for N atoms in the $AO7^-$ moiety; iii) with Fe-L-IMO, larger Fe_2O_3 clusters likely hinder $AO7^-$ adsorption.

Introduction

The term nanotube (NT), come into usage since about two decades, is universally associated with Carbon NT [1], one of the most studied chemical object today. Other materials, with the same features of hollow elongated rods, have been since prepared [2-4], though not often with the same amazing difference in size in one direction. Less known (in the practice only known to experts of clay-type materials) is the fact that alumino-silicate NTs of the same fascinating geometry of CNTs can be synthesized, besides being present in nature.

Indeed, imogolite (IMO) is a hydrated alumino-silicate with formula $(OH)_3Al_2O_3SiOH$ [5,6] either found in volcanic soils or prepared by sol-gel synthesis [7-9]. Bridged Al(OH)Al groups, with octahedrally (Oh) coordinated Al atoms, occur at NTs outer surface (which has amphoteric nature, [10]) and non-interacting silanols (SiOH) at the inner surface (Scheme 1).

The length of a single IMO NT varies between 400 nm and several microns, whereas the inner diameter is constant at 1.0 nm [10]. The outer diameter is *ca.* 2.0 in natural IMO, whereas it varies around 2.5-2.7 nm in synthetic samples, due to the presence of different inter-tubes impurities [6]. IMO NTs arrange in bundles with nearly hexagonal packing.

This structure gives rise to three kinds of pores [11,12] and surfaces, as reported in Scheme 2 [13]: (i) pores A are intra-tubes pores, 1.0 nm in diameter, lined by silanols, the related A surface being very hydrophilic and able to interact with H_2O, NH_3 and CO [13,14]; (ii) pores B, 0.3-0.4 nm wide, are those among three aligned NTs within a bundle, hardly accessible even to small molecules like water [11,12]; (iii) pores C are slit mesopores among bundles, the surface of which may interact with larger molecules, like phenol [10] and 1,3,5-triethylbenzene [13].

The interest in IMO-related chemistry has spread recently, one reason being the possibility of changing the composition of both inner and outer surface of NTs. The former can be modified in several ways: (i) by substitution of Si atoms by Ge atoms, NTs are given rise with formula $(OH)_3Al_2O_3Si_{1-x}Ge_xOH$, with inner diameter of 2.0 nm [15], shorter than IMO NTs, and either

3

single or double walled [16]; (ii) by grafting organic functionalities at the inner surface of IMO, $(OH)_3Al_2O_3SiO$-R NTs result, where R is the organic group [17]; (iii) by properly choosing the Si precursor, hybrid NTs with formula $(OH)_3Al_2O_3Si$-R (R = -CH_3, -CH_2-NH_2) [18,19] form by direct synthesis.

Modification of the outer surface involves either electrostatic interaction or covalent bonding. The latter occurs in the reaction between pre-formed IMO and an organo-silane, like 3-aminopropylsilane [20]; the former exploits the charge matching between the outer surface of NTs and a proper counter-ion, like octadecylphosphonate [21]. This is possible since in water the outer and inner surface of NTs are charged because of the following equilibria [22]:

$$Al(OH)Al \; + \; H^+ \; = \; Al(OH_2)^+Al \qquad (1)$$

$$SiOH \; = \; SiO^- \; + \; H^+ \qquad (2)$$
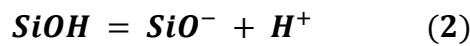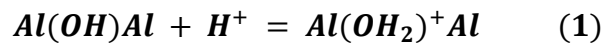
The same equilibria may be exploited in several applications, the most straightforward being anions/cations retention from polluted water by electrostatic interaction with the charged surface of NTs [23-27].

The present work concerns yet another modification of the outer surface, the isomorphic substitution of Oh Al^{3+} by Fe^{3+}, hereafter referred to as Al^{3+}/Fe^{3+} IS. Though being a common process in all natural alumino-silicates, less is known about Fe-doped IMO. The presence of Fe^{3+} may impart the solid new chemical and solid-state properties, but the nature and the electronic effects generated by Al^{3+}/Fe^{3+} IS are not fully understood, so far. Theoretical calculations showed that iron could either isomorphically substitute for aluminium or create "defective sites" both inside and outside IMO NTs [28]. Such defects, *i.e.* iron oxo-hydroxide particles, could be able to reduce the band gap of IMO (an electrical insulator) from 4.7 eV to 2.0-1.4 eV [28].

The first experimental studies on Fe-doped IMO [29,30] indicated that there is an upper limit to the amount of iron, in that NTs are preserved up to an overall 1.4 wt % iron content. More recent reports on Fe-doped aluminium-germanate NTs, isostructural with IMO, showed that iron

isomorphic substitution is indeed limited to 1.0 wt %, and formation of iron oxo-hydroxides unavoidably occurs at higher Fe content [31].

Concerning ions removal from polluted water, no studies are available on the adsorption properties of Fe-doped IMO, besides a paper regarding yet other materials, *i.e.* imogolite-Fe_3O_4 (magnetite) composites, of which the behaviour towards arsenate anions adsorption from polluted water was studied [32].

In this work, two samples were synthesized with 1.4 wt % Fe content (the maximum amount of iron that allows to preserve NTs structure according to ref. 29 and 30), by adopting either direct (Fe-x-IMO) or post-synthesis (Fe-L-IMO) procedures. The adopted procedure for the direct synthesis differed, *inter alia*, in the silicon and aluminium precursors from the already reported method [29,30] that employed $NaSiO_4$ and $AlCl_3$, instead of Tetraethoxysilane and Al-*sec*-butoxide, respectively. The post-synthesis loading was carried out with the purpose of obtaining a reference material with iron occurring only as oxo-hydroxide species. On the ground of results in ref. 31, a sample with a lower iron content (0.7 wt %) was obtained by direct synthesis, in order to get a material in which mainly, if not only, Al^{3+}/Fe^{3+} IS occurred. In the latter case, formation of Fe(OH)Al groups, replacing some Al(OH)Al groups at the outer surface of NTs, is expected (Scheme 1b), which could modify the adsorption properties of the outer surface of IMO NTs (eq. 1).

Morphological and textural properties of the three Fe-doped IMO are here compared to those of proper IMO. In addition, surface properties related to Fe(OH)Al groups are studied in water, by measuring the ζ potential and the interaction with the (bulky) anion of the azo-dye Acid Orange 7 (NaAO7). The latter was chosen as a probe of the outer surface of NTs for two principal reasons: i) it is a model molecule for the many azo-dyes found as contaminants of both wastewater and groundwater [33]; ii) in virtue of its molecular dimensions (Scheme 3) is expected to mainly interact with the outer surface of NTs, limiting parasitic interactions possibly deriving by diffusion within IMO inner pores [34].

Experimental Section

Materials and synthetic procedures.

Acid Orange 7 (NaAO7, Scheme 3), was from Fluka, all other reagents were Sigma-Aldrich ACS grade.

IMO was obtained as reported elsewhere [10]. Fe-x-IMO samples were obtained by direct synthesis as follows: in a glove box, a proper amount of $FeCl_3*6H_2O$ was added to 20 mM solution of $HClO_4$, then TEOS (tetraetoxysilicate) and Al-sec-butoxide were added, the pH of the resulting mixture being = 4.0. The aqueous mixture was stirred at room temperature for 18h, diluted to 20 mM in Al, autoclaved at 100 °C for 4 days, filtered, washed and dried overnight at 50 °C in oven. A reddish-brown powder was obtained, the solution recovered by filtration being instead transparent.

Fe-L-IMO was prepared by contacting proper amounts of IMO and $FeCl_3*6H_2O$ in water (resulting pH = 4.0) for 24 h under stirring and finally adding NH_4OH solution (33% by weight) to precipitate all Fe^{3+} as oxo/hydroxide. The solid was filtered, washed and dried in oven at 50 °C overnight.

Methods.

Electron micrographs were obtained on a Jeol 3010-UHR high resolution transmission electron microscope (HRTEM) operating at 300 kV, equipped with a LaB_6 filament and with an Oxford Inca Energy TEM 300 EDS X-rays analyser (Oxford Link) for atomic recognition. Digital micrographs were acquired by a (2k x 2k)-pixel Ultrascan 1000 CCD camera and processed by Gatan digital micrograph. Before the experiments, the samples, in the form of powders, were milled in an agate mortar and deposited on a copper grid covered with a lacey carbon film.

Powder X-Ray Diffraction (XRD) patterns were obtained on a X'Pert Phillips diffractometer operating with Cu Ka radiation (1.541874 Å) in the 2.5 – 18° 2θ range (step width = 0.02°, time per step: 2.00s).

Samples thermal stability under inert flow (either Ar or N_2) was studied by Thermo-Gravimetric (TG) analysis (heating rate: 10 degrees min-1). Data reported below indicate that the structure is stable up to 250 °C, a temperature hereafter assumed for successive thermal treatments.

To determine BET SSA (Brunauer-Emmett-Teller Specific Surface Area) and porous volume values reported in Table 1, N_2 isotherms were measured at -196°C on samples previously outgassed at 250 °C, in order to remove water and other atmospheric contaminants, still preserving NT structure [10,35] . NL-DFT (Non Local Density Functional Theory Method) was used to determine Pores Size Distributions (PSDs) in Figure 3b, by using a N_2-silica kernel for cylindrical pores. Diffuse Reflectance (DR) UV-Vis spectra of outgassed samples were measured on a Cary 5000 UV-Vis-NIR spectrophotometer (Varian instruments). The same instrument was used in the transmission mode for $NaAO_7$ adsorption measurements.

For IR measurements, samples were shaped as self-supporting, thin wafers (20 mg cm^{-2}) and outgassed at 250 °C in a standard vacuum frame (residual pressure below 10^{-3} mbar) to remove water. Adsorption of ammonia was studied at room temperature (r.t.) on such dehydrated samples by using a home-made IR cell in quartz equipped with (IR transparent) KBr windows.

Electrophoretic mobility as a function of pH was measured at 25°C by means of electrophoretic light scattering technique on a Zetasizer Nano-ZS instrument (Malvern Instruments, Worcestershire, UK). The corresponding ζ-potential curves were calculated according to the Henry's equation: $U_E = 2\varepsilon\zeta f(K_a)/3\eta$, where U_E is the electrophoretic mobility, ε is the dielectric constant, ζ is the zeta potential, $f(K_a)$ is the Henry's function, and η is the viscosity. The adopted value of $f(K_a)$ was 1.5, in agreement with the Smoluchowski approximation, usually applied to aqueous solutions of moderate electrolyte concentration, as in the present case. Water suspensions were obtained after 2 min sonication with an ultrasonic probe (100 W, 20 kHz, Sonoplus; Bandelin, Berlin, Germany); the pH of the suspension was then adjusted by adding either 0.10 M HCl or 0.10 M NaOH.

Adsorption of NaAO7 was studied by contacting powder suspensions (1g L^{-1}) with a 0.67 mM NaAO7 water solution (starting pH value of 6.80): the supernatant solution was recovered by centrifugation and analysed at regular time intervals by transmission UV-Vis spectroscopy with a 1 mm path cuvette.

Results and discussion

Physico-chemical characterization of the materials

Figures 1a, 1b and 1c report, respectively, the TEM images of a whole IMO particle, a magnification of a bundle of parallel NTs, and a detail of the terminal region of a bundle, showing a hexagonal array of NTs.

Such morphological features were preserved in all the Fe-containing samples, irrespectively of both synthesis procedure and Fe amount (Figures 1d-1l). Moreover, EDS maps of the Fe-containing samples (Figures SM1-SM3) showed a homogenous distribution of Fe, indicating the effectiveness of both synthesis procedures. Arrows in Figure 1h point out the occurrence of some iron-containing clusters at the outer surface of NTs in Fe-L-IMO sample. Their average size was evaluated by electron micrographs acquired at 50,000 magnification, in which the clusters were clearly detectable, resulting well contrasted with respect to the IMO structure. The histogram of the particle size distribution in Fig. 1h was obtained by considering 450 particles on the TEM images, and their average particle diameter, $d_m \sim 4.4$ nm, was calculated as $d_m = \Sigma d_i n_i / \Sigma n^i$, where n_i was the number of particles of diameter d_i. Such particles, hardly detectable in Fe-0.70-IMO, were also present in Fe-1.4-IMO, though having a slightly smaller average diameter ($d_m \sim 4.0$ nm). Such differences in cluster size were, however, meaningful, being able to modify the magnetic susceptibility of the materials, as reported in a previous work [36].

The formation of a hexagonal packing of NTs is confirmed by XRD patterns in Fig. 2: the peaks observed with IMO, Fe-0.70-IMO, Fe-1.4-IMO, and Fe-L-IMO all correspond to the hexagonal

array so clearly visible in Fig. 1. The vertical bar in Fig. 2 shows that the d_{100} diffraction is at different position in curves 3 and 4: the peak is at $2\theta = 3.88°$ with both IMO and Fe-L-IMO (vertical bar), and at slightly higher 2θ values with both Fe-0.70-IMO ($2\theta = 4.03°$) and Fe-1.4-IMO ($2\theta = 4.06°$). Accordingly, the cell parameter a, which depends on d_{100} ($\boldsymbol{a = 2d_{100}/\sqrt{3}}$), is 2.62 nm with both IMO and Fe-L-IMO and 2.51 nm with both Fe-x-IMO samples (Table 1).

Scheme 2 shows that a corresponds to the distance between the centre of two adjacent NTs, and actually depends on both the NTs diameter and the distance between two neighbouring NTs.

Upon Al^{3+}/Fe^{3+} IS, NTs inner diameter should increase, as showed by EPR measurements [36] indicating the occurrence of isolated Oh Fe^{3+} species in high-spin state, which have a Shannon radius of 0.645 Å definitely larger than Oh Al^{3+} (0.535 Å). If so, the change in a values should be related to a decreased distance between neighbouring NTs.

Evidence of a larger inner diameter comes from N_2 adsorption measurements and in particular by PSDs curves below reported. Isotherms in Figure 3a show the expected shape for a microporous system with some mesoporosity (Table 1). Note that Fe-L-IMO has a larger mesopores volume, because the loading procedure mainly affects the C surface, by formation of iron oxo-hydroxide nanoclusters observed by HRTEM.

PSDs curves in Fig. 3b show a slight increase in diameter in the sequence IMO = Fe-L-IMO < Fe-0.70-IMO < Fe-1.4-IMO: absolute values are not entirely worth of trust, being lower than 1.0 nm, but the trend is most probably reliable. Further support comes from the HRTEM analyses: internal pores diameter, carefully measured on several images on both IMO and Fe-x-IMO samples, showed an increase in the series IMO (1.05 nm) < Fe-0.70-IMO (1.29 nm) < Fe-1.4-IMO (1.34 nm) (Figure SM4).

On the ground of the aforementioned result, the smaller a values for Fe-x-IMO samples, as opposed to the larger internal diameter, is most likely due to a decreased distance between adjacent NTs, which is affected by the anions present in the synthesis bath, not entering though the IMO formula.

9

In natural samples, the *a* value may vary between 2.0 and 2.7 nm, without any change in inner diameter, because of the different impurities possibly present within inter-nanotubes spaces. With IMO, previous work [37] has indeed shown the occlusion of some perchlorate anions coming from the synthesis batch, because the release of molecular oxygen at high temperature was observed by TG-mass analysis. During the synthesis of Fe-x-IMO, chloride ions likely replace (larger) perchlorate anions, so decreasing the final *a* value. Indeed, thermal treatment of both Fe-x-IMO samples did not show any release of oxygen, as measured by TG-Mass analysis reported in Fig. SM5 and SM6.

Thermal stability is an important issue in view of possible applications, since IMO tends to release water by dehydroxylation with formation of a lamellar phase: Al^{3+}/Fe^{3+} IS may affect the thermal stability, as well as the presence of different anions joining adjacent NTs.

The DTG curves in Fig. 4 show with all the samples a mass loss in the 30 – 250 °C range, due to desorption of molecular water that extends up to relatively high temperatures, because of the difficult diffusion of water molecules within very hydrophilic A pores. With IMO (curve 1), two other mass losses are observed at *ca.* 350°C, due to dehydroxylation of Al(OH)Al groups [18], and at *ca.* 420°C, due to SiOH condensation, with consequent NTs collapse and formation of a lamellar phase [35,37].

With all Fe-doped samples, only one mass loss is observed at about 350 °C: XRD patterns of samples treated at 500°C (Figure SM7) show that a lamellar phase is formed, so indicating that the presence of Fe probably accelerates dehydroxylation. Such effect is observed also with Fe-L-IMO: this indicates that Al^{3+}/Fe^{3+} IS likely occurs also by post-synthesis procedure, as confirmed by DR-UV-Vis spectra in Fig. 5.

IMO has, as expected, a negligible absorption in the UV-Vis region (curve 1, in Fig. 5), whereas the Fe-doped samples show similar, though not equal, UV-Vis features. Both Fe-x-IMO samples (curves 2 and 3) strongly absorb at 270 nm, and show a minor absorption band at 480 nm, almost negligible with Fe-0.70-IMO, in agreement with the almost nihil formation of clusters. According to

the literature, the former signal is due to charge-transfer transitions (CT) from O^{2-} to isolated Oh Fe^{3+} ions, the latter to d-d transitions of Fe^{3+} in Fe_2O_3 clusters [38]. Fe-L-IMO spectrum (curve 4) is similar to that of Fe-1.4-IMO, though slightly shifted to higher wavelengths and more intense in the region of d-d transitions. This is ascribed to the formation of slightly larger Fe_2O_3 clusters by post-synthesis method [36], although Fe-L-IMO also absorbs at 270 nm.

At 1.4 wt % Fe content, both isolated Oh Fe^{3+} species and aggregated Fe-O-Fe groups are obtained: magnetic susceptibility measurements showed indeed that Al^{3+}/Fe^{3+} IS substitution was limited to *ca.* 0.9 % wt Fe [36], then Fe_2O_3 clusters formed, in fair agreement with what observed with Fe-doped Ge-imogolite [31], and with the natural tendency of iron to form Fe-O-Fe bridges in non acidic media [39]. On the one hand, UV-Vis spectra show that formation of Fe_2O_3 is not completely avoided by direct synthesis, on the other hand, evidence is given of the occurrence of some Al^{3+}/Fe^{3+} IS during the loading procedure. The Al^{3+}/Fe^{3+} IS was also confirmed by the narrowing of the band gap in the three Fe-containing imogolite, as reported elsewhere [36].

The presence of isolated Oh Fe^{3+} sites (band at 270 nm) in Fe-L-IMO indicates that ionic exchange occurred between structural Oh Al^{3+} in pre-formed IMO and Fe^{3+} ions in water:

$$[Al(OH)^+Al](s) + Fe(H_2O)_6^{3+} = [Fe(OH)^+Al](s) + Al(H_2O)_6^{3+} \qquad (3)$$
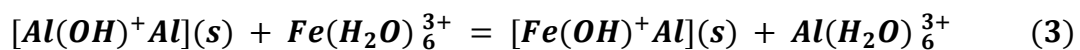
The latter is an interesting result, since it opens to the possibility of changing the composition of IMO outer surface by ionic exchange with proper ions, avoiding more difficult procedures like direct synthesis.

Roughly assuming that Al^{3+}/Fe^{3+} IS was the main process occurring in Fe-0.70-IMO, such material would have chemical formula $(OH)_3Al_{1.975}Fe_{0.025}O_3SiOH$ and therefore an $Al^{3+}/Fe^{3+} = 79$ molar ratio, indicating a high dilution of Oh Fe^{3+} sites. Examination of Scheme 1b shows, indeed, that upon Al^{3+}/Fe^{3+} IS three Fe(OH)Al species are formed around the same Fe ion, so that the amount of

such species would be higher and able to actually modify the surface properties of IMO, in particular the hydroxyls population of the outer surface.

Figure 6 compares IR spectra of the bare samples after dehydration at 250 °C: in the 3800-2700 cm^{-1} range a broad absorption is observed due to H-bonded hydroxyls [10]. With IMO (curve 1), bands are seen 1595 and 1465 cm^{-1} assigned to carbonate-like species similar to those formed at the surface of aluminium hydroxide [40]: their intensity decreases in the series Fe-L-IMO > Fe-0.70-IMO > Fe-1.4-IMO (curves 3, 2 and 4, respectively), in agreement with the fact that the outer surface is progressively losing its aluminium-hydroxide character as far as Al^{3+}/Fe^{3+} IS takes place.

No other differences may be appreciated in Fig. 6, because of the relatively low Fe content and the plethora of hydroxyls occurring both within and outside NTs, especially with Fe-0.70-IMO, its IR spectrum being very similar to that of proper IMO.

Figure 7 reports IR spectra obtained upon ammonia adsorption on dehydrated samples: since difference spectra are reported (as obtained after subtraction of spectra of the bare samples in Fig. 6), the observed negative/positive bands are respectively due to species disappearing/forming upon NH_3 dosage. Ammonia is able to interact with both inner and outer surface of nanotubes [13]. With IMO (Fig. 7a), the negative band at 3735 cm^{-1} is mainly ascribed to inner SiOH interacting by H-bonding with NH_3 [10, 13]. At lower wavenumbers, the bands at 1625 cm^{-1} and 1450 cm^{-1} are respectively due to the bending mode of NH_3 molecules coordinated by Lewis sites (outer Al^{3+}) and of NH_4^+ ions formed by reaction with (less abundant, defective) hydroxyls, more acidic than inner SiOH [10,13].

Fig. 7b compares difference IR spectra in the N-H bending range obtained with the four samples under the same equilibrium pressure of NH_3: the spectra of IMO (1) and Fe-0.70-IMO (2) are very similar, likely due to the low Fe content of the latter. With Fe-L-IMO (3), another component is observed at 1485 cm^{-1}, due to NH_4^+ ions formed by interaction with weakly acidic OH groups, likely related to Fe_2O_3 clusters. With Fe-1.4-IMO (4), the component at 1475 cm^{-1} is

amenable to NH_4^+ ions formed by interaction with Fe(OH)Al groups, having an intermediate acidic character between Al(OH)Al and Fe_2O_3-related hydroxyls.

Fig. 7c-f compare difference IR spectra in the OH region, at two different NH_3 partial pressures. As already mentioned, with IMO the dominant SiOH species is characterized by a band at 3735 cm^{-1} (Fig. 7c): the same band is also observed with the Fe-containing samples. With Fe-0.70-IMO (Fig. 7d) no relevant differences are observed in the OH range, in agreement with the low Fe content, whereas with Fe-1.4-IMO a new OH species at 3720 cm^{-1} is observed (Fig. 7e), ascribed to Fe-(OH)-Al groups. With Fe-L-IMO such band is absent, notwithstanding the presence of isolated Fe^{3+} ions documented above, and a new band is observed at 3705 cm^{-1} (Fig. 7f), due to hydroxyls species related to Fe_2O_3 clusters: such OH groups should be less acidic, and indeed the band due to ammonium ions is less intense in Fe-L-IMO (curve 3, Fig. 7b). The absence of the 3720 cm^{-1} band in Fe-L-IMO seems to indicate that several Fe-(OH)-Al groups act as condensation centres for other Fe^{3+} ions, ending in the formation of larger Fe_2O_3 clusters [36]].

Samples behaviour in water

Figure 8 reports ζ potential curves for samples IMO, Fe-1.4-IMO and Fe-L-IMO, as IR spectroscopy did not noticed any relevant difference in the surface properties of Fe-0.70-IMO with respect to IMO. In agreement with the literature, IMO (squares) is positively charged at low pH, the point of zero charge (PZC) being at pH = 9.8, a value close to those reported for alumina [41,42]. This result is in agreement with the chemical nature of its external surface, exposing only Al-O-Al groups and Al(OH)Al bridges, like a hydrated aluminium oxide. The curve for Fe-1.4-IMO (triangles) lies below that of IMO over nearly the whole range of pH values, *i.e.* the sample is less positively charged in water: we take this as evidence that Fe(OH)Al are slightly less acidic than Al(OH)Al in water and, indeed, the PZC is marginally different. The same holds for Fe-L-IMO, *i.e.* hydroxyl of iron oxo-hydroxide nanoclusters are less acidic in water than Al(OH)Al species: error bars show that the net difference in surface charge is not relevant, in that the samples are positively

charged at low pH, and negatively charged at higher pH, so they should be able to adsorb anions in a similar way at low pH

Some differences, however, emerged concerning the properties of the outer surface of NTs, which could affect adsorption properties of iron-doped IMO. To this respect, Figure 9 describes the adsorption experiments of NaAO7, the UV spectrum of which is reported in Scheme 3b: the hydrazone form of $AO7^-$, stable in the solid phase, undergoes an azo-hydrazone tautomerism, via an intra-molecular proton transfer, so that both hydrazone and azo-form are simultaneously present in water. The two bands at 310 and 230 nm and the shoulder at 256 nm are due to aromatic rings absorptions. The band at 484 nm is due to the n-π* transition involving the lone pair on N atoms and the conjugated system extending over the two aromatic moieties and encompassing the N-N group of the hydrazone form [43,44]. The shoulder at 403 nm has a similar nature, involving this time the N-N group of the azo form.

Figure 9a reports the UV-Vis spectra of the liquid phase after 120 min contact with the studied samples: in the reported experiments, no new bands form with respect to the starting solution, indicating that a mere adsorption process occurs. From the obtained adsorption data, the trend in intensities concerning the four samples reported in Figure 9b is evaluated, whereas section c of the Figure shows the parallel behaviour of the solution pH.

Fig. 9b shows with Fe-1.4-IMO a steep increase in the percentage of $AO7^-$ removal: within 30 min, a plateau is reached corresponding to removal of *ca.* 95 % $AO7^-$. Fe-0.70-IMO shows a curve with a similar shape, though the amount of removed $AO7^-$ is lower. With IMO, the curve has a different shape, indicating the occurrence of two processes, a faster one within the first 30 min, followed by a slower one. The shape of Fe-L-IMO curve is a similar to that of IMO, but the overall amount of removed $AO7^-$ is smaller. Different curves shape indicates that different adsorption processes occur. With Fe-1.4-IMO, a strong interaction should occur between the dye and outer Fe^{3+} ions. The interaction is strong, in that $FeAO7^-$ adducts form, not by electrostatic interaction, but by coordination of Fe^{3+} ions by N atoms of the organic dye, through ligand displacement. Simple

stoichiometric calculation shows an $AO7^-/Fe^{3+}$ molar ratio of 3/1, indicating that probably after one FeAO7$^-$ adduct forms, other dye molecules are adsorbed by the latter species. With IMO, such process does not occur, and the steep increase observed in Fig. 9b within the first 30 min is ascribed to AO7$^-$ moieties electrostatically interacting with the (positively charged) outer surface. The process occurring at longer times is ascribed to another phenomenon, like the slow diffusion of AO7$^-$ molecules within IMO A pores (*vide infra*). The adsorbing behaviour of Fe-L-IMO is similar to that of IMO, indicating that the adsorption process is again electrostatic interaction. The lower adsorption capacity of Fe-L-IMO as compared to IMO may be ascribed to the presence, at the outer surface of NTs, of larger Fe_2O_3 clusters [36], on which AO7$^-$ molecules cannot adsorb, as reported by the literature [33].

The simultaneous pH change is reported in Fig. 9c: two processes are seen to occur, *i.e.* one rapid, involving a steep decrease in pH, the other one time-dependent, and implying a moderate pH increase.

The slow process is most probably related to the difficult diffusion of NaAO7 into A-type pores, the size of which is of the order of the transverse dimension of AO7$^-$: the interaction is with inner silanols through a process that decreases the concentration of hydronium ions in the solution. The fast process, instead, takes place at the outer C surface, involving either Al(OH)Al or Fe(OH)Al species, and causes the release of hydronium ions in solution. With Fe-1.4-IMO, the latter process is particularly relevant.

As it concerns IMO, the following reactions seem to account for the features observed:

$$SiO^- + H^+ + AO7^- = SiOH \cdots AO7^- \qquad (4)$$

$$Al(OH_2)^+Al + AO7^- = Al(OH)Al \cdots AO7^- + H^+ \qquad (5)$$
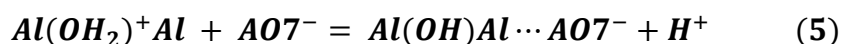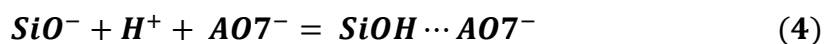
The adsorption process implies hydrogen bonding of the AO7$^-$ anion with acidic hydroxyls, silanols and bridged species, respectively. This implies in turn reversal of eqns. (1) and (2), with opposite

variations in pH. Simple stoichiometric calculation on the initial pH drop of IMO shows, however, that reaction (5) contributes to the removal of *ca.* 5 % of AO7$^-$ molecules, indicating that the interaction between AO7$^-$ and the outer surface of IMO NTs is mainly electrostatic.

With Fe-1.4-IMO, and to a minor extent also with Fe-0.70-IMO, a second interaction may take place with Fe(OH$_2$)$^+$Al groups:

$$Fe(OH_2)^+Al \ + AO7^- = FeAO7^- + AlOH + H^+ \qquad (6)$$

Reaction (6) likely implies the formation of FeAO7$^-$ adducts, not by electrostatic interaction, but by coordination of Fe^{3+} ions by N atoms of the organic dye, through a ligand displacement phenomenon. However, reaction (6) contributes to the removal of a minor fraction of AO7$^-$ molecules, indicating that actually only a small fraction of Fe(OH)Al groups is protonated (*ca.* 2 %, as calculated on the basis of stoichiometric considerations).

On the contrary, with Fe-L-IMO such Fe(OH)Al groups mainly served as crystallization centres for the growth of iron oxo-hydroxide nanoclusters and are no more available to bind to AO7$^-$ species, finally lowering the adsorption capacity of Fe-L-IMO (Fig. 9b) and giving rise to moderate changes in pH (Fig. 9c).

The above results are interesting since with Fe-1.4-IMO about 90 % dye is removed from solution within 5 min, since by their nature of transition element, Fe^{3+} ions can display coordinative capacity towards N atoms of AO7$^-$. This means that transition metal-doped IMO could be able to remove organic contaminants from polluted water, not only inorganic ions, as already reported for magnetite-imogolite composite materials able to remove arsenate ions with high efficiency [32].

Conclusions

16

Fe-doped IMO NTs may be obtained by either direct synthesis or post-synthesis procedure. The former method is more complicated, since it implies the perturbation of the synthesis mixture by addition of the iron precursor, and allows mere Al^{3+}/Fe^{3+} IS only at low iron content, as observed with Fe-0.70-IMO sample.

At higher iron content, the Fe(OH)Al groups formed at NTs outer surface likely act as seeds for the unavoidable formation of Fe_2O_3 clusters, as also observed in Fe-doped aluminium-germanate imogolite-like NTs [31]. However, this does not lead to the loss of NTs structure, that is preserved at 1.4 wt % Fe, in agreement with pioneering papers on the subject [29, 30]. Unexpectedly, the post-synthesis loading procedure led to some Al^{3+}/Fe^{3+} IS, meaning that isomorphic substitution may occur by cation exchange, through a simpler procedure, by contacting IMO with an aqueous solution of Fe^{3+} and, probably, also with other trivalent cations with suitable size.

The main effects of the presence of Fe are on (i) thermal stability of NTs, in that NTs collapse is slightly accelerated by Fe^{3+} ions, likely inducing some additional strain in the curved walls of NTs and (ii) formation of Fe(OH)Al bridged groups. The latter are slightly less acidic than Al(OH)Al groups, but provide accessible Fe^{3+} sites that in water may be accessible to species able to coordinate iron, as observed in the case of $AO7^-$, finally leading to a higher efficiency towards the retention of such moiety. This concept could be extended to retention of other organic pollutants containing ligands able to coordinate Fe^{3+} or other transition metal cations replacing outer Al^{3+} species by ionic exchange of pre-formed IMO. This way it will be possible to exploit the outer surface of NTs for adsorption processes not only implying mere electrostatic interactions, but ligand displacement, as well.

Table 1. Samples textural properties as derived by N_2 sorption isotherms at -196 °C and low angles XRD patterns.

Sample	Fe wt%	BET SSA, $m^2\,g^{-1}$	Pore Total Volume, $cm^3\,g^{-1}$	[a]Micro-pore Volume,$cm^3\,g^{-1}$	$d_{100,}$ nm (±0.01)	[b]$a,$ nm
IMO	-	383	0.21	0.13	2.27	2.62
Fe-L-IMO	1.4	400	0.27	0.13	2.27	2.62
Fe-0.70-IMO	0.7	450	0.22	0.15	2.19	2.53
Fe-1.4-IMO	1.4	455	0.22	0.14	2.17	2.51

a) As obtained by applying the *t*-plot method.

b) Cell parameter, *a*, as calculated by applying the eq. $a \; = \; 2d_{100}/\sqrt{3}$

Captions to Figures

Figure 1. HRTEM images of an IMO bundle (a), formed by parallel NTs (b) forming a hexagonal array (c). HRTEM images taken with Fe-0.70-IMO (sections d and e); Fe-1.4-IMO (sections f and g) and Fe-L-IMO (sections h-l). Insert to section h: particle size distribution of iron-containing nanoclusters obtained with Fe-L-IMO. The instrumental magnification was 10000X in section a, and 50000X in all the other sections.

Figure 2. Low angles XRD patterns of IMO (1), Fe-L-IMO (2), Fe-0.70-IMO (3), and Fe-1.4-IMO powder samples.

Figure 3. Section a: N_2 sorption isotherms at -196 °C of IMO (squares), Fe-L-IMO (circles), Fe-0.70-IMO (stars) and Fe-1.4-IMO (triangles) samples dehydrated at 250 °C. Full and hollow symbols refer to adsorption and desorption branches, respectively. Section b: Pore size distributions of IMO (squares), Fe-L-IMO (circles), Fe-0.70-IMO (stars) and Fe-1.4-IMO (triangles) as obtained by applying the NL-DFT method.

Figure 4. Differential Thermo-Gravimetry (DTG) curves of IMO (1), Fe-L-IMO (2), Fe-0.70-IMO (3), and Fe-1.4-IMO (4) samples, as obtained under Ar atmosphere, in the 30-500 °C temperature range.

Figure 5. DR UV-Vis spectra of IMO (1), Fe-0.70-IMO (2), Fe-1.4-IMO (3) and Fe-L-IMO (4).

Figure 6. IR spectra of IMO (1), Fe-0.70-IMO (2), Fe-L-IMO (3), and Fe-1.4-IMO (4) samples dehydrated at 250 °C.

Figure 7. Section a: difference IR spectra obtained after dosing NH_3 at r.t. on IMO dehydrated at 250 °C. NH_3 equilibrium pressure in the 0.50-30 mbar range. Section b: difference IR spectra obtained with IMO (1), Fe-0.70-IMO (2), Fe-L-IMO (3) and Fe-1.4-IMO (4) under *ca.* 10.0 mbar ammonia. Sections c-f: difference IR spectra, in the OH stretching region, as obtained after dosing NH_3 at r.t. on IMO (c), Fe-0.70-IMO (d), Fe-L-IMO (e) and Fe-1.4-IMO (f) samples. NH_3

equilibrium pressure corresponding to 2.5 and 10 mbar. Differences were obtained by subtracting IR spectra of bare samples reported in Fig. 6.

Figure 8. ζ potential curves of IMO (squares), Fe-1.4-IMO (triangles) and Fe-L-IMO (circles).

Figure 9. Section a: UV-Vis spectra of the starting AO7 solution (1) and of the supernatant solutions after 120 min in contact with Fe-L-IMO (2), Fe-0.70-IMO (3), IMO (4), and Fe-1.4-IMO (5). Section b: percentage of AO7 removed by IMO (squares), Fe-L-IMO (circles), Fe-1.4-IMO (triangles) and Fe-0.70-IMO (stars). Section c: pH of the solutions during AO7 adsorption measurements.
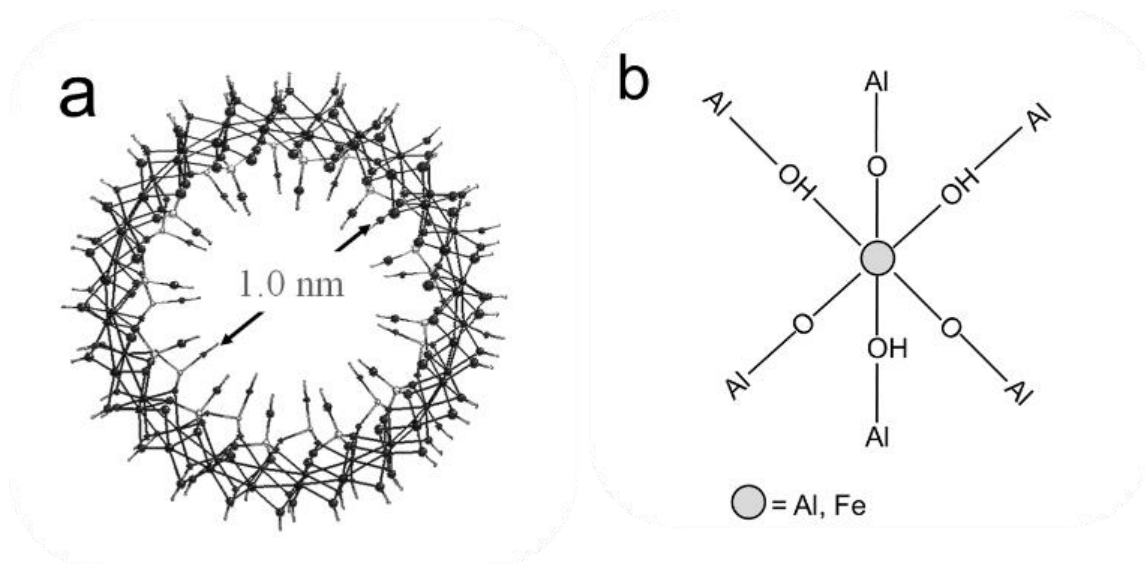
Scheme 1. Section a: front view of an IMO nanotube, with an inner diameter of 1.0 nm and exposing SiOH and Al(OH)Al groups at the inner and outer surface, respectively. Section b: environment surrounding each octahedral cation (either Al^{3+} or Fe^{3+}) at the external surface of NTs.
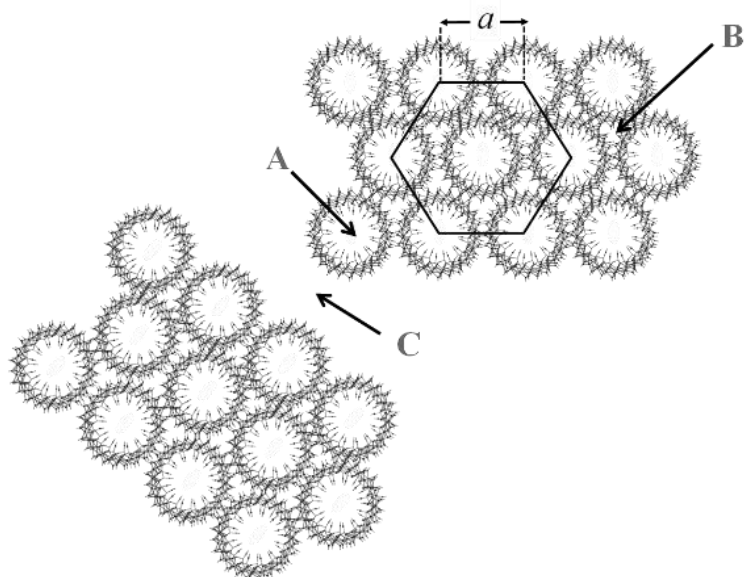
Scheme 2. IMO NTs hexagonally packed in bundles. The cell parameter a corresponds to the distance between the centres of two NTs within a bundle. Pores A, B and C correspond to proper IMO nanopores (Ø = 1.0 nm); pores among three aligned NTs (Ø = 0.3 nm) and (disordered) slit mesopores between bundles, respectively [8].
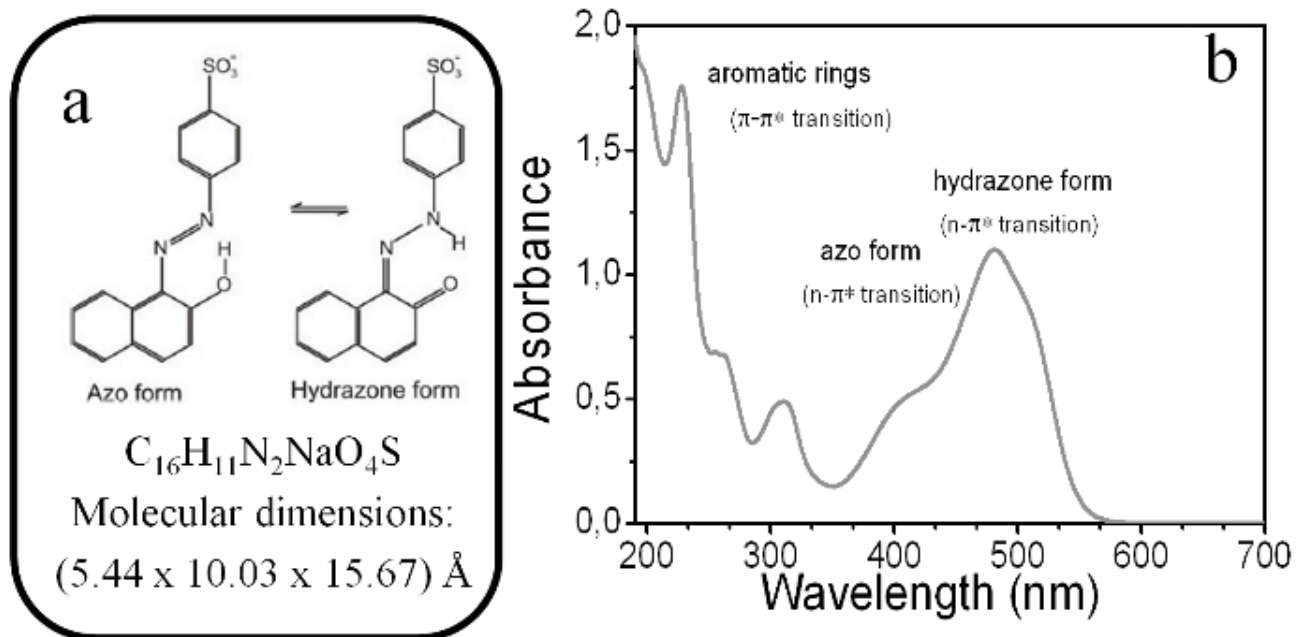
Scheme 3. Part a): structure formula and molecular dimensions [34] of AO7⁻. Part b: UV-Vis spectrum of 0.67 mM AO7 aqueous solution: absorption bands due to both the azo- and hydrazone forms of the dye are observed.
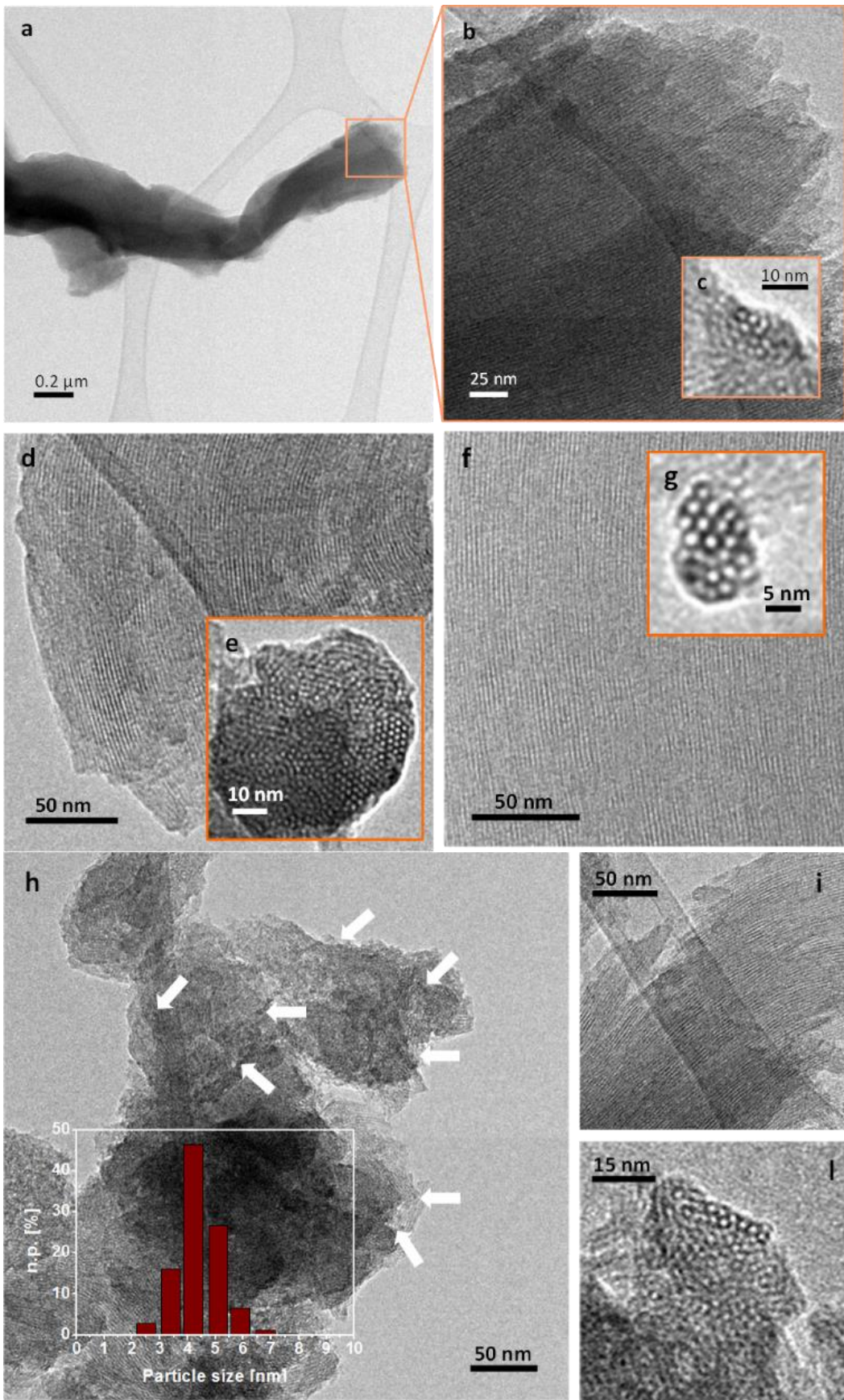
Figure 1. E. Shafia et al.

23
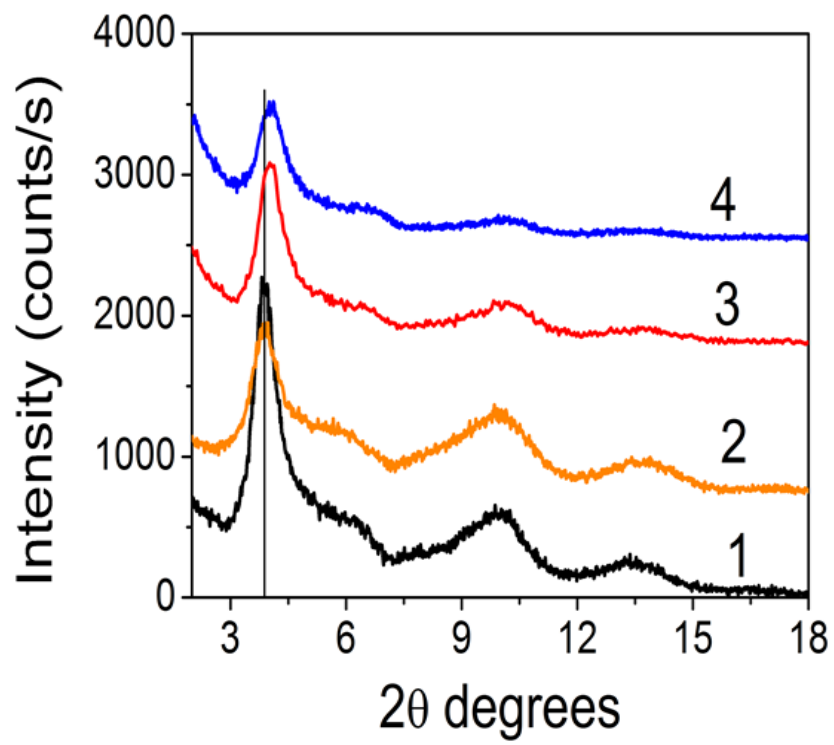
Figure 2. E. Shafia et al.
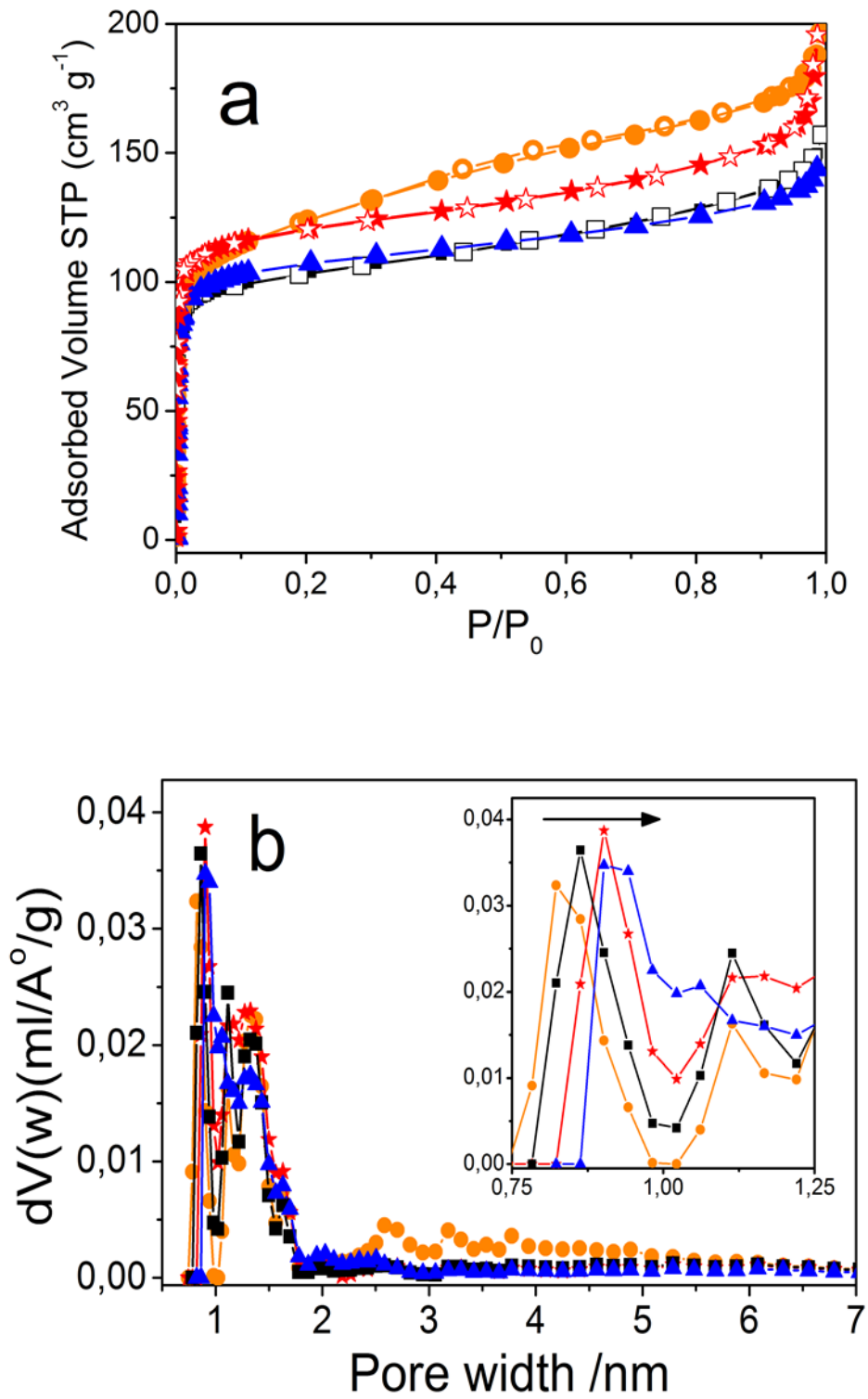
Figure 3. E. Shafia et al
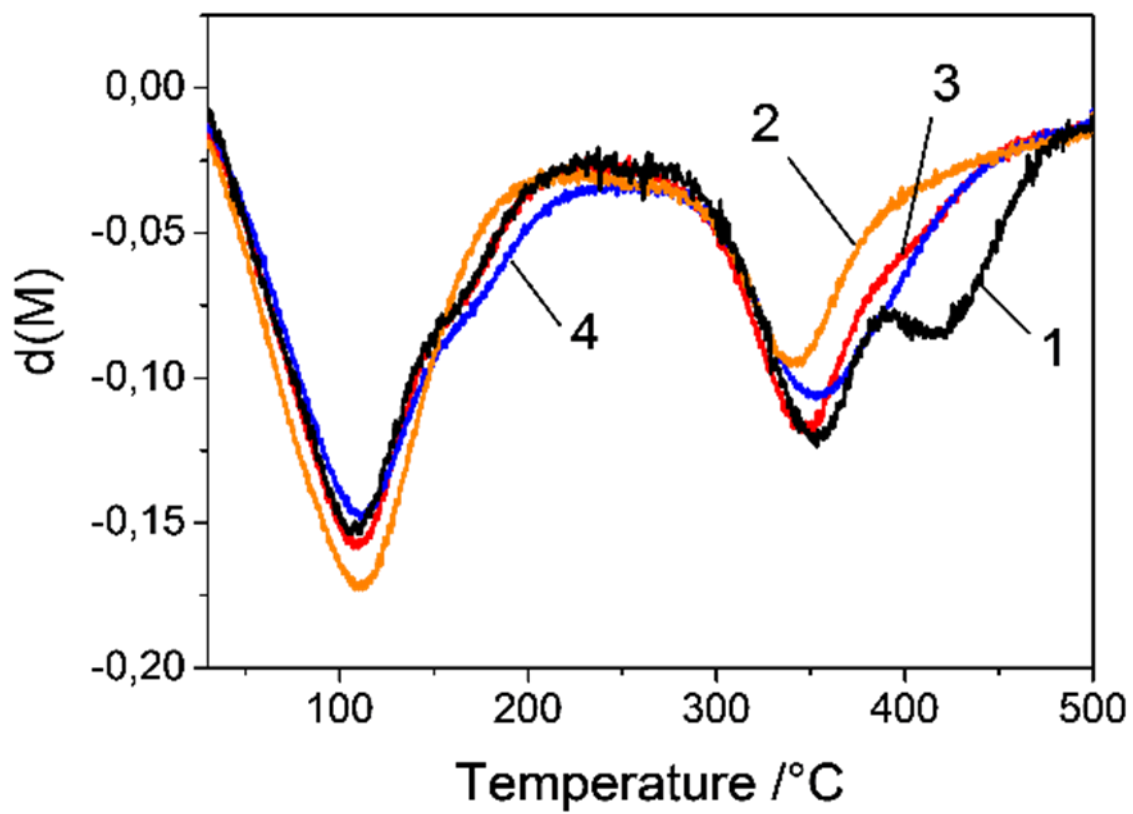
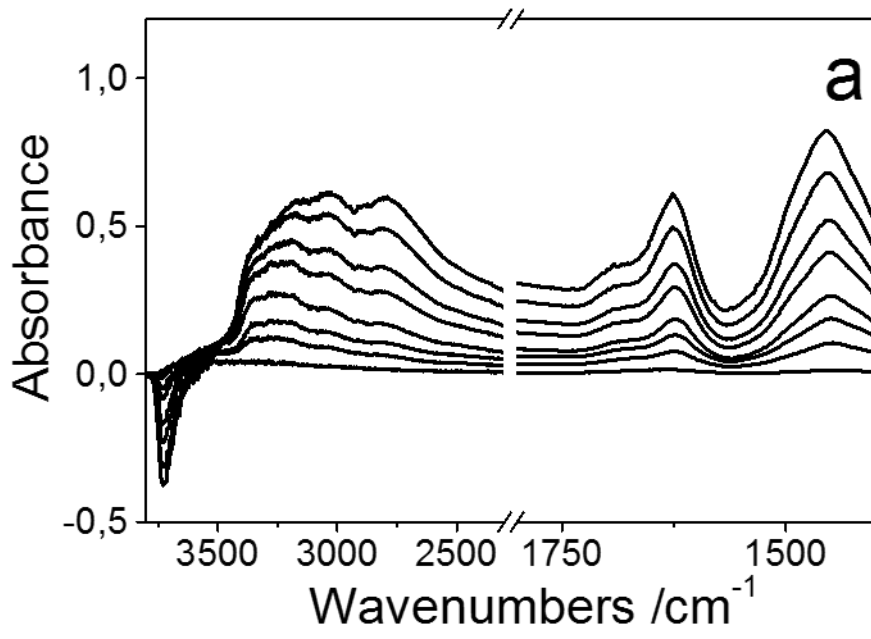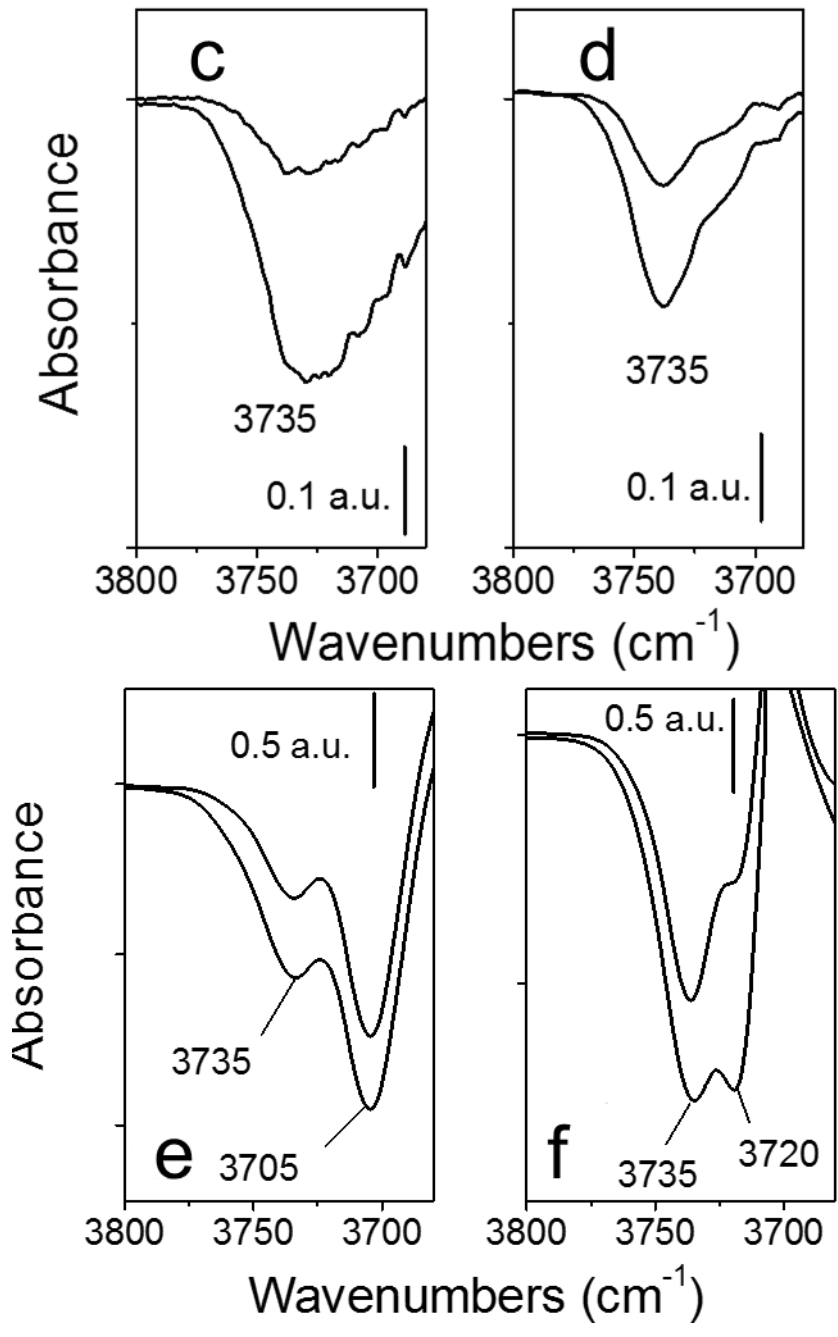*Figure 4. E. Shafia et al.*
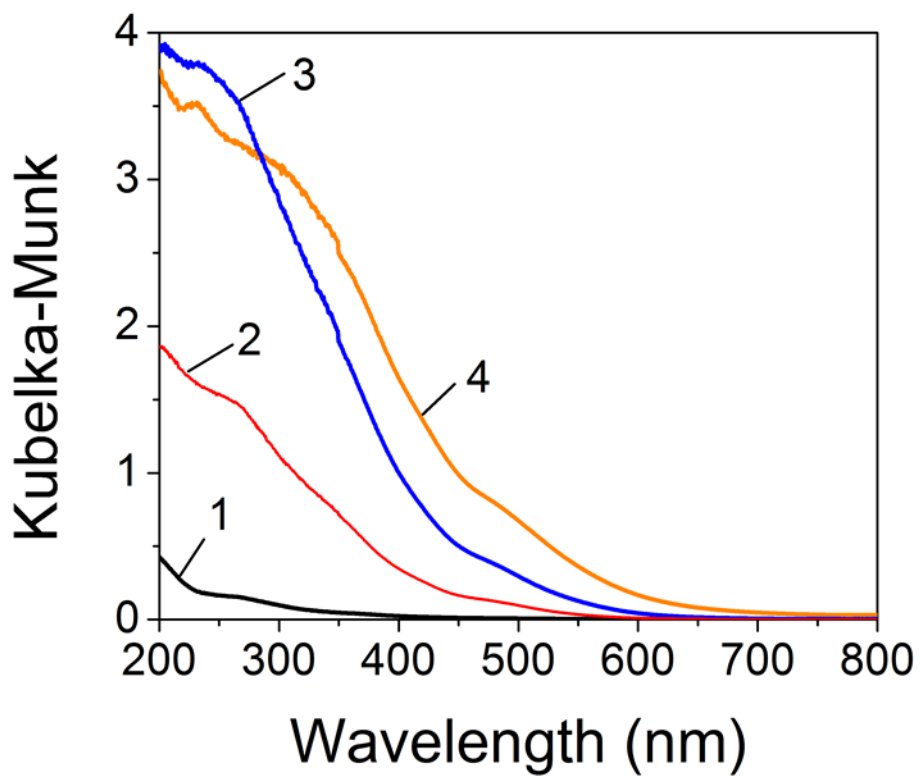
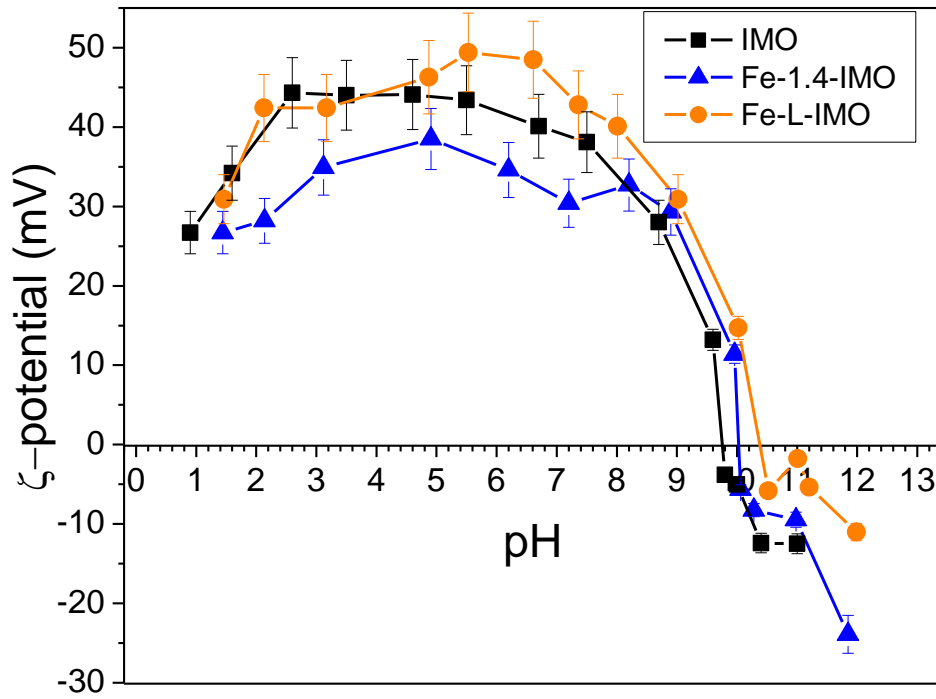*Figure 5. E. Shafia et al.*
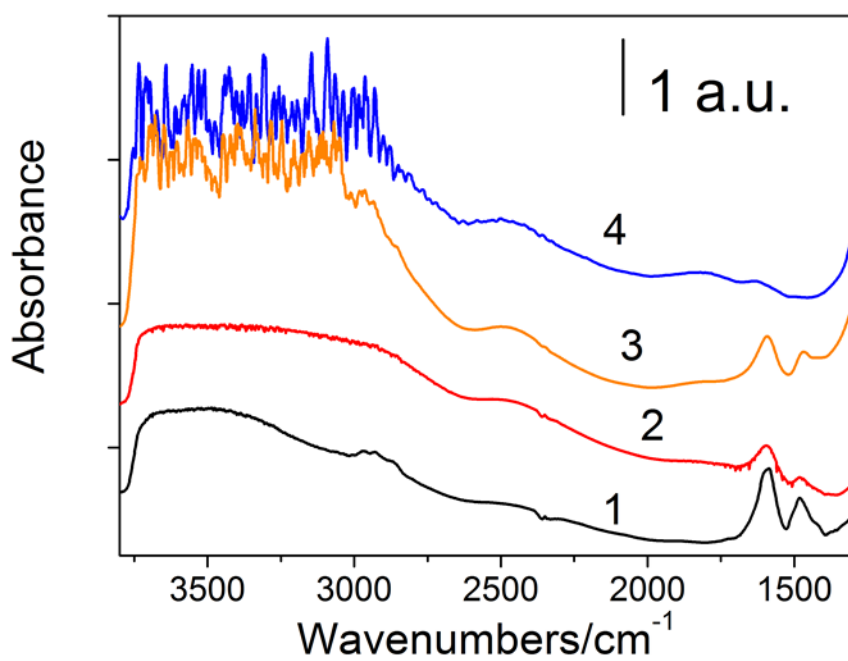
Figure 6 E. Shafia et al..
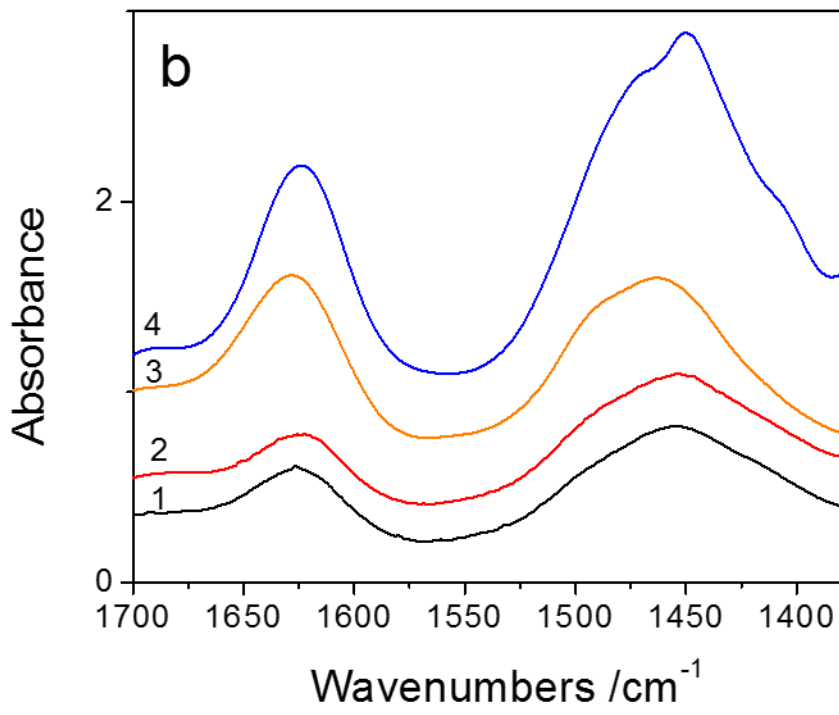
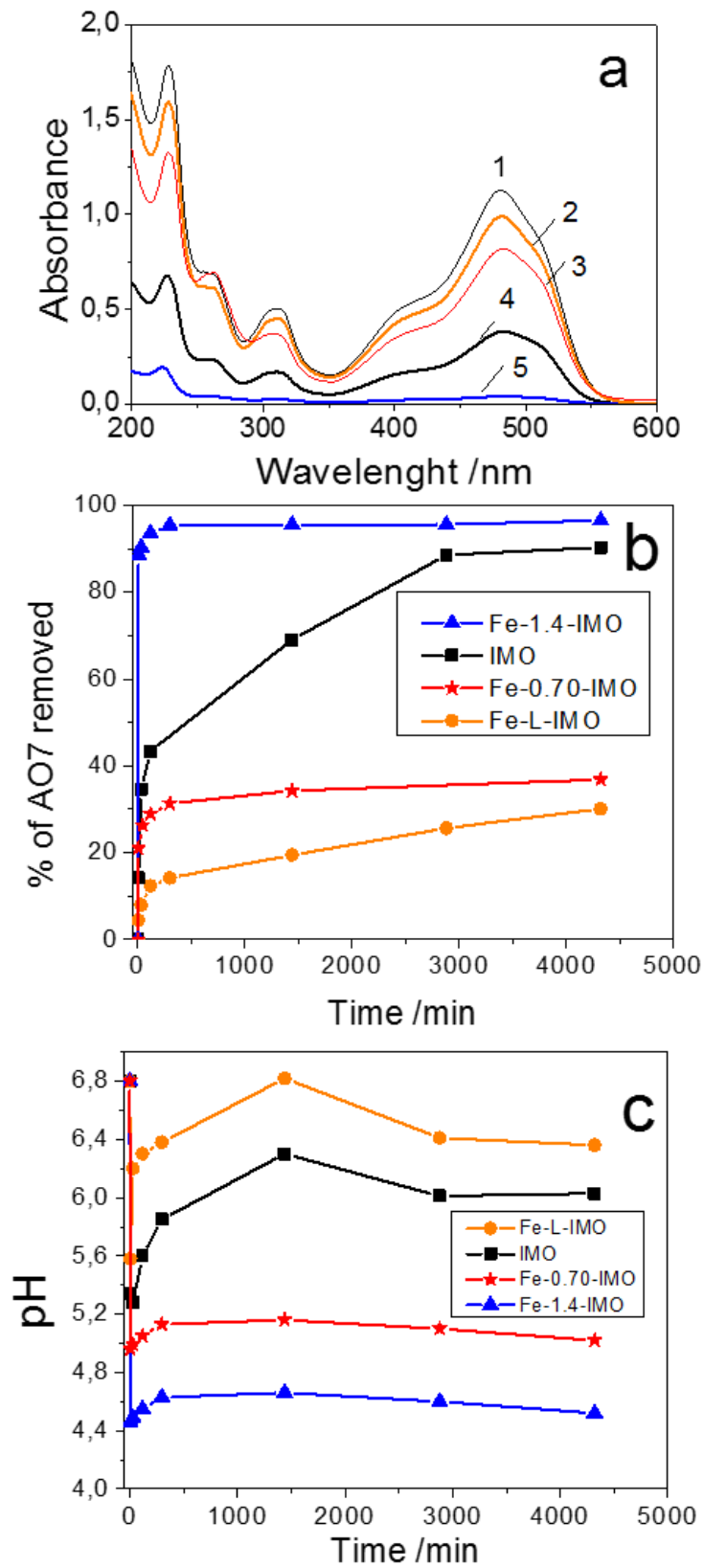*Figure 7 E. Shafia et al..*

Figure 8 E. Shafia et al..

Figure 9. E. Shafia et al.

31

References

[1]   P.M. Ajayan, Chem. Rev. 99 (1999) 1787–1800.

[2]   K. Lee, A. Mazare, P. Schmuki, Chem. Rev. 114 (2014) 9385–9454.

[3]   R.K. Joshi, J.J. Schneider, Chem. Soc. Rev. 41 (2012) 5285–5312.

[4]   J.H. Jung, M. Park, S. Shinkai, Chem. Soc. Rev. 39 (2010) 4286–4302.

[5]   N.Yoshinaga, A. Aomine, Soil Sci. Plant Nutr. 8 (1962) 22–29.

[6]   P.D.G. Cradwick, V.C. Farmer, J.D. Russell, K. Wada, N. Yoshinaga, Nature Phys. Sci. 240 (1972) 187–189.

[7]   V.C. Farmer, A.R. Fraser in: M. M. Mortland, V. C. Farmer (Eds.). Synthetic Imogolite: a tubular hydroxyaluminium silicate. Proceedings of the International Clay Conference, Elsevier, Amsterdam, 1978, pp. 547–553.

[8]   S.I. Wada, A. Eto, K. Wada, J. Soil. Sci. 30 (1979) 347–355.

[9]   V.C. Farmer, M.J. Adams, A.R. Fraser, F. Palmieri, Clay Miner. 18 (1983) 459–472.

[10]   B. Bonelli, I. Bottero, N. Ballarini, S. Passeri, F. Cavani and E. Garrone, J. Catal. 264 (2009) 15–30.

[11]   W.C. Ackerman, D.M. Smith, J.C. Huling, Y. Kim, J.K. Bailey, C.J. Brinker, Langmuir 9 (1993) 1051–1057.

[12]   M.A. Wilson, G.S.H. Lee, R.C. Taylor, Clays Clay Miner. 50 (2002) 348–351.

[13]   B. Bonelli, M. Armandi, E. Garrone, Phys. Chem. Chem. Phys. 15 (2013) 13381–13390.

[14]   S.I. Wada, K. Wada, Clays Clay Miner. 30 (1982) 123–128.

[15]   S. Mukherjee, V.M. Bartlow,S. Nair, Chem. Mater. 17 (2005) 4900–4909.

[16]   A. Thill, P. Maillet, B. Guiose, O. Spalla, L. Belloni, P. Chaurand, M. Auffan, L. Olivi, J. Rose, J. Am. Chem. Soc. 134 (2012) 3780–3786.

[17]   D-Y. Kang, J. Zang. C.W. Jones, S. Nair, J. Phys. Chem. C 115 (2011) 7676–7685.

[18]   I .Bottero, B. Bonelli, S. Ashbrook, P. Wright, W. Zhou, M. Tagliabue, M. Armandi, E. Garrone, Phys. Chem. Chem. Phys. 13 (2011) 744–750.

[19]   D-Y. Kang; N.A. Brunelli, G.I. Yucelen, A. Venkatasubramanian, J. Zang. J. Leisen, P.J. Hesketh, C.W. Jones, S. Nair, Nature Commun. 5 (2014) 3342.

[20]   C. Zanzottera, A. Vicente, E. Celasco, C. Fernandez, E. Garrone, B. Bonelli, J. Phys. Chem. C 116 (2012) 7499–7506.

[21]   S. Park, Y. Lee, B. Kim, J. Lee, Y. Jeong, J. Noh, A. Takahara, D. Sohn, Chem. Commun. (2007) 2917–2919.

[22]   J.P. Gustafsson, Clays Clay Miner. 49 (2001) 73–80.

[23]   L. Denaix, I. Lamy, J.Y. Bottero, Colloids Suf. A 158 (1999) 315–325.

[24]   C. J. Clark, M.B. McBride, Clays Clay Miner. 32 (1984) 291–299.

[25]   R. L. Parfitt, A.D. Thomas, R.J. Aktinson, R.St.C. Smart, Clays Clay Miner. 22 (1974) 455–456.

[26]   Y. Arai, M. McBeath, J.R. Bargar, J. Joye, J.A. Davis, Geochim. Cosmochim. Acta 70 (2006) 2492–2509.

[27]   J. B. Harsh, S. J. TRaina, J. Boyle, Y. Tang, Clays Clay Miner. 40 (1992) 700–706.

[28]   F. Alvarez-Ramírez, J. Chem. Theory Comput. 5 (2009) 3224–3231.

[29]   M. Ookawa, Y. Inoue, M. Watanabe, M. Suzuki, T. Yamaguchi, Clay Sci. 12 (2006) 280–284.

[30]   M. Ookawa, in "Clay Minerals in Nature - Their Characterization, Modification and Application" InTech 2012, 239–258.

[31]   A. Avellan, C Levard, N Kumar, J Rose, L Olivi, A Thill, P Chaurand, D Borschneck, A Masion, RSC Advances 4 (2014) 49827–49830.

[32]   N. Arancibia-Miranda, M. Escudey, C. Pizarro, L.C. Denardin, M.T. García-González, J.D. Fabris, L. Charlet, L., Mater. Res. Bull. 51 (2014) 145-152.

[33] F. S. Freyria, B. Bonelli, R. Sethi, M. Armandi, E. Belluso, E. Garrone, J. Phys. Chem. C 115 (2011) 24143–24152.

[34] X. Zhao, X. Bu, T. Wu, S.-T. Zheng, L. Wang, P. Feng, Nature Commun. 4 (2013) 2344.

[35] K.J. MacKenzie, M.E. Bowden, J.W.M. Brown, R.H. Meinhold, Clay Clay Miner. 37 (1989) 317–324.

[36] E. Shafia. S. Esposito, M. Manzoli, M. Chiesa, P. Tiberto, S. Barrera, G. Menard, P. Allia, F.S. Freyria, E. Garrone, B. Bonelli, J. Nanopart. Res. 17 (2015) 336.

[37] C. Zanzottera, A. Vicente, M. Armandi, C. Fernandez, E. Garrone, B. Bonelli, J. Phys. Chem. C 116 (2012) 23577–23584.

[38] Y. Wang, Q.H. Zhang, T. Shishido, K. Takehira, J. Catal. 209 (2002) 186–196.

[39] R. Stösser, G. Scholz, Appl. Magn. Reson. 15 (1998) 449–468.

[40] C. Morterra, G- Magnacca, Catal. Tod. 27 (1996) 497-532.

[41] B.M. Rotoli, P. Guidi, B. Bonelli, M. Bernardeschi, M.G. Bianchi, S. Esposito, G. Frenzilli, P. Lucchesi, M. Nigro, V. Scarcelli, M. Tomatis, P.P. Zanello, B. Fubini, O. Bussolati, E. Bergamaschi, Chem. Res. Tox. 27 (2014) 1142–1154.

[42] H.-Y. Shu, M.-C. Chang, H.-H. Hu, W.-H. Chen, J. Colloid Interface Sci. 314 (2007) 89–97.

[43] J.A. Mielczarki, G.M. Atenas, E. Mielczarski, Appl. Catal. B 56 (2005) 289–303.

[44] C. Bauer, P. Jacques, A. Kalt, J. Photochem. Photobiol. A 140 (2001) 87–92.

Supplementary Material

Isomorphic substitution of aluminium by iron into single-walled alumino-silicate nanotubes: new physico-chemical insights into the structural and adsorption properties of Fe-doped imogolite.

Ehsan Shafia,[1] Serena Esposito,[2] Marco Armandi,[1] Maela Manzoli,[3] Edoardo Garrone,[1] Barbara Bonelli[1,*]

[1] *Department of Applied Science and Technology and INSTM Unit of Torino Politecnico, Corso Duca degli Abruzzi 24, Politecnico di Torino, Turin, Italy.*

[2] *Department of Civil and Mechanical Engineering, Università degli Studi di Cassino e del Lazio Meridionale, Via G. Di Biasio 43, 03043 Cassino (FR), Italy.*

[3] *Department of Chemistry & NIS Interdepartmental Centre, University of Turin, Via P. Giuria 7, 10125 Turin, Italy*

* Corresponding author: Tel. +39 011 0904719 Fax. +39 011 0904624; *e-mail*:

barbara.bonelli@polito.it (Prof. Barbara Bonelli).
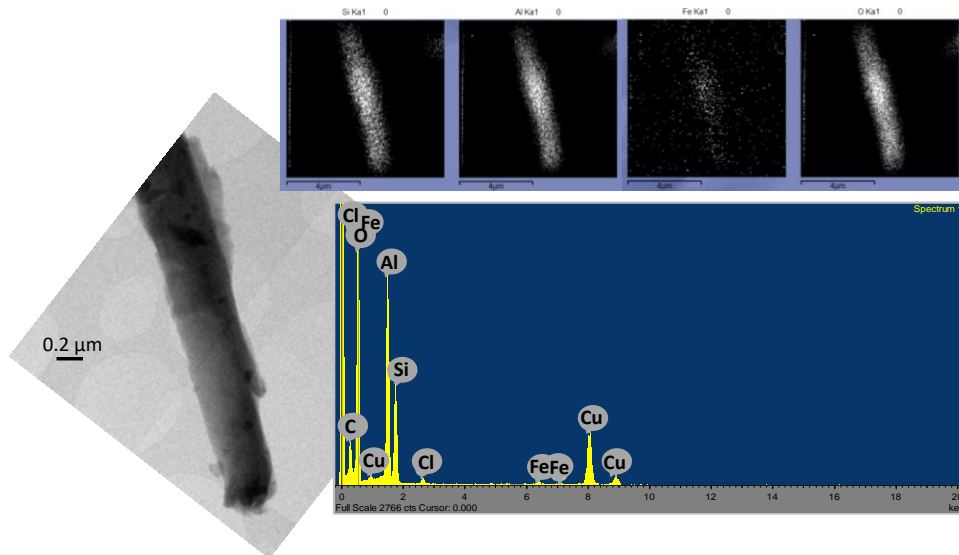
1. *EDS maps of Fe-containing samples*

Figure SM1. Left figure: HRTEM image of a Fe-0.70-IMO bundle. Corresponding EDS maps allowing the speciation of Si, Al, Fe and O elements (top right figures) and EDS spectrum (bottom right figure). Instrumental magnification: 8000X.
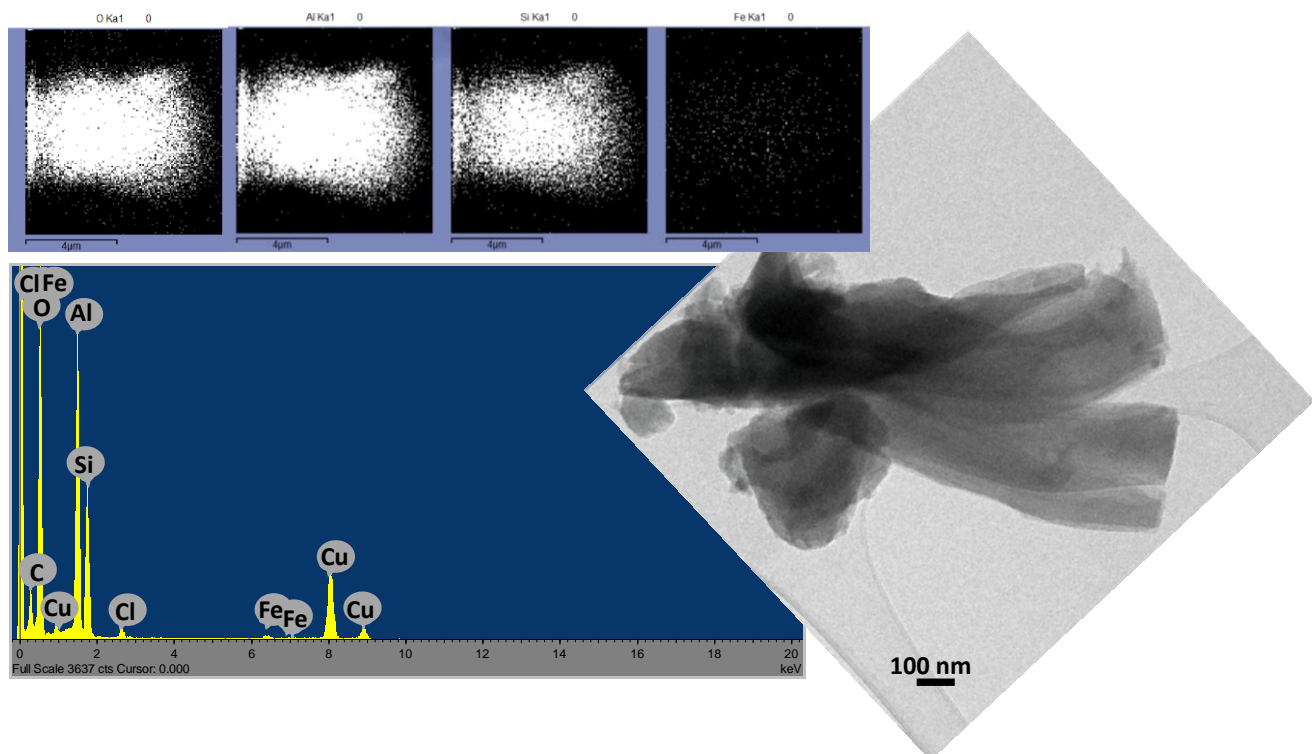
Figure SM2. HRTEM image of Fe-1.4-IMO bundles (right figure). EDS map of the same region allowing speciation of O, Al, Si and Fe elements (top left figures) and EDS spectrum collected on the bundles. Instrumental magnification: 15000X.
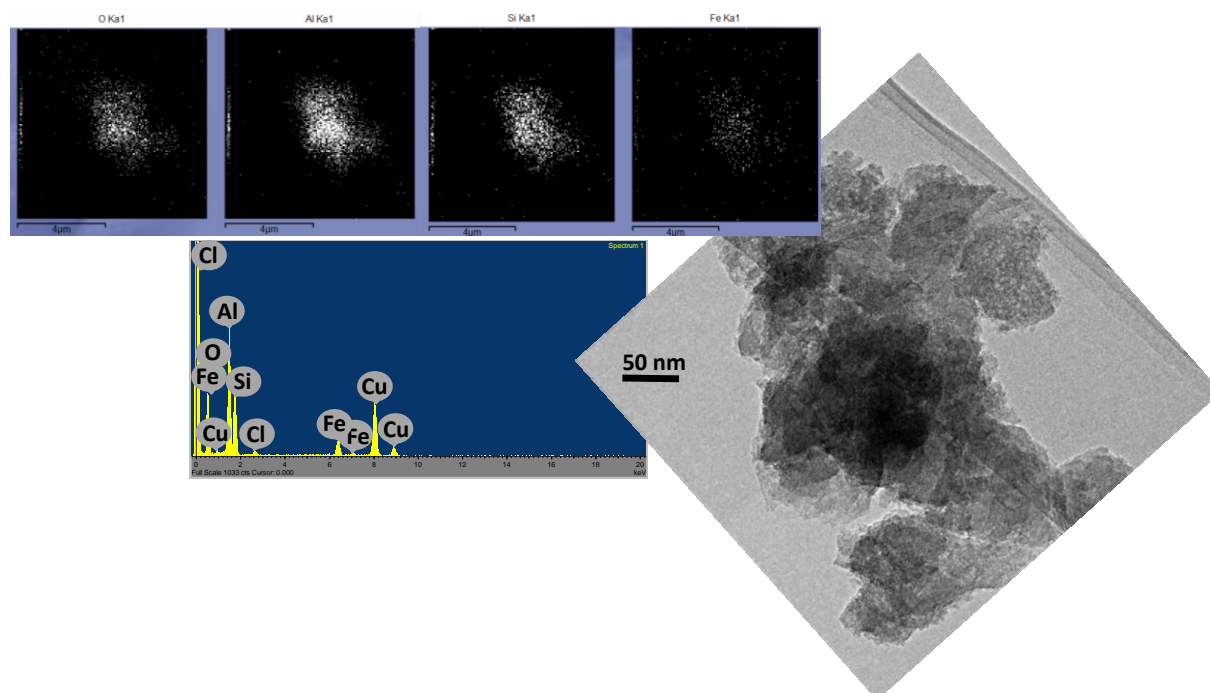

Figure SM3. HRTEM image of Fe-L-IMO (right figure), EDS map of the same region allowing speciation of O, Al, Si and Fe elements (top left figures) and EDS spectrum collected on the bundles (bottom left figure). Instrumental magnification: 50000X.

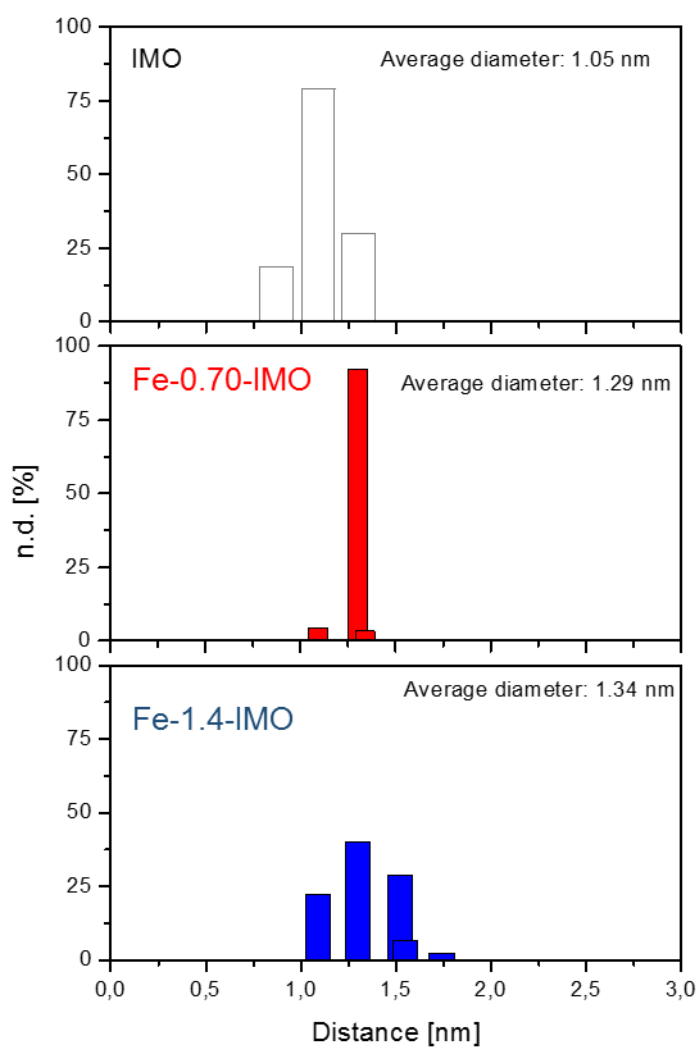*2. Pores diameter distribution as obtained by HRTEM analysis.*

Figure SM4. Diameter distributions of IMO, Fe-0.70-IMO and Fe-1.4 -IMO as

obtained by HRTEM analysis.
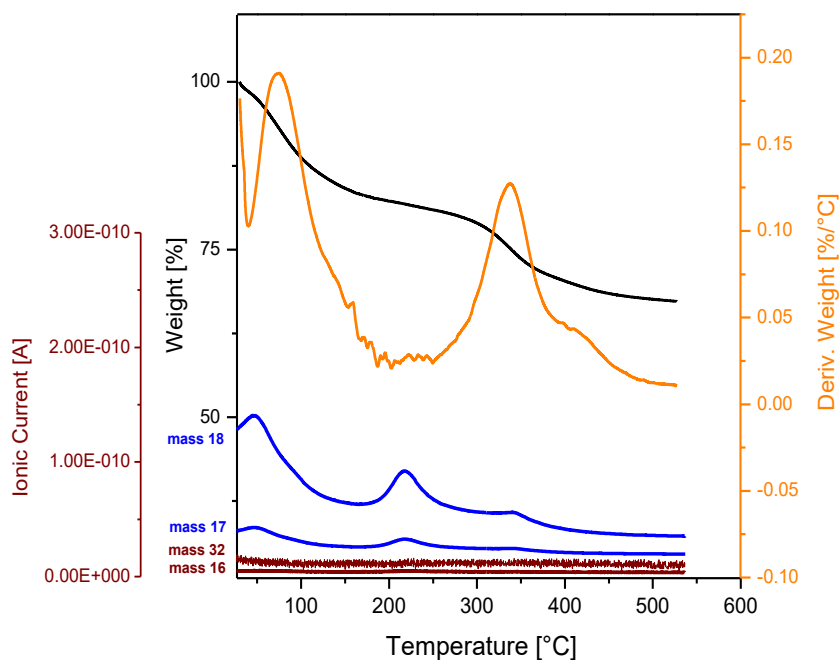
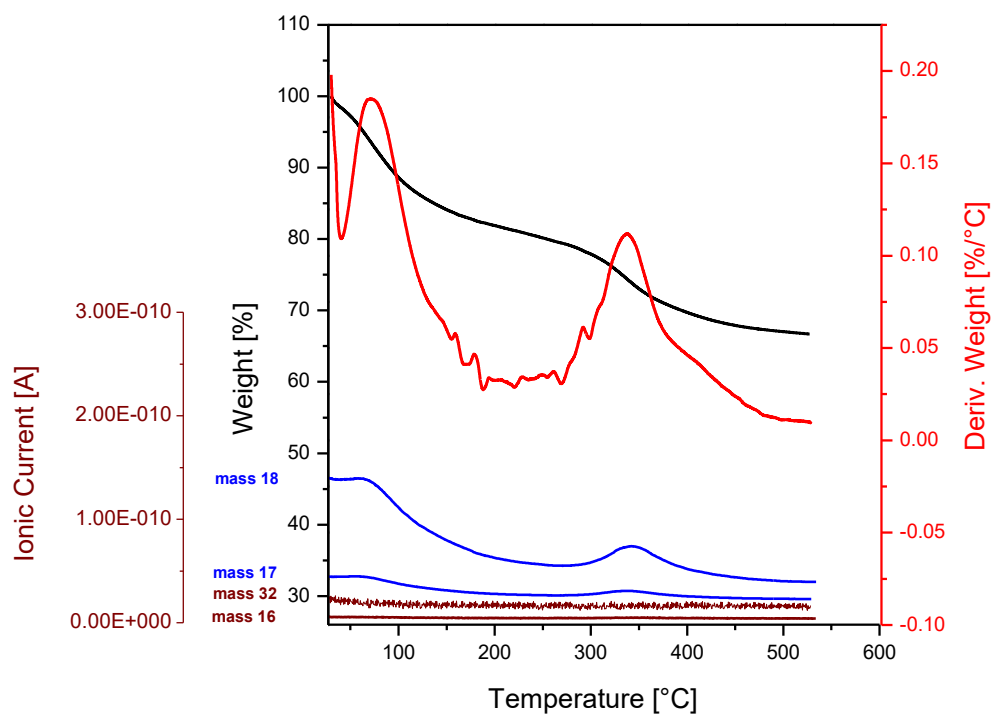## 3. TG-Mass analysis of Fe-0.70-IMO and Fe-1.4-IMO

Figure SM5. Thermo-Gravimetry (TG) and Differential Thermo-Gravimetry (DTG) curves of Fe-0.70-IMO, as obtained under N_2 atmosphere in the 30-530 °C temperature range combined with quadrupole mass spectroscopy monitoring both O_2 and H_2O related masses.

Figure SM6. Thermo-Gravimetry (TG) and Differential Thermo-Gravimetry (DTG) curves of Fe-1.45-IMO, as obtained under N_2 atmosphere in the 30-530 °C temperature range combined with quadrupole mass spectroscopy monitoring both O_2 and H_2O-related masses.

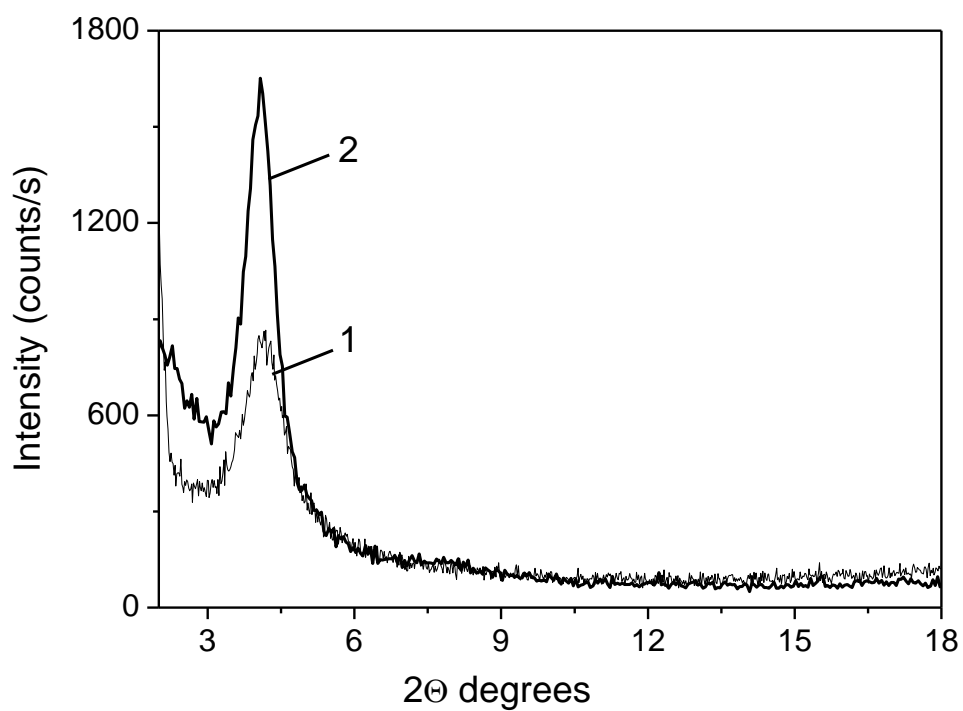*4. Powders XRD patterns of IMO and Fe-1.4-IMO after thermal treatment at 500°C.*

Figure SM7. XRD patterns of IMO (1) and Fe-1.4-IMO (2) after thermal treatment at 500 °C.

Only one peak is observed in XRD patterns reported Figure S7, showing in both cases the formation of a lamellar phase due to NTs collapsing after thermal treatment at 500 °C.